



Contents lists available at ScienceDirect

Journal of Sound and Vibration

journal homepage: www.elsevier.com/locate/jsv

A multisynchrosqueezing-based high-resolution time-frequency analysis tool for the analysis of non-stationary signals

Gang Yu

School of Electrical Engineering, University of Jinan, Jinan 250022, China

ARTICLE INFO

Article history:

Received 23 February 2020
Revised 11 October 2020
Accepted 23 October 2020
Available online xxx

Keywords:

Time-frequency analysis
Synchrosqueezing transform
Bearing fault diagnosis
Time-varying signal analysis

ABSTRACT

In this paper, a high-resolution time-frequency (TF) analysis method is presented for the analysis of strongly non-stationary signals. TF representations generated by conventional methods are usually too blurry to provide precise features for such signals. A recently proposed method, called multisynchrosqueezing transform (MSST), overcomes most of the problems that exist in conventional methods, which seems to be a promising tool. However, the MSST still has a major problem, i.e., non-reassigned point problem, which may lead to the blurry energy problem for some special TF points. This paper mainly focuses on resolving this problem. This study finds that such a problem in the MSST is caused by the rounding operation in the discrete procedure of the reassigned step. An effective method is then employed to address this problem using a simple strategy. Additionally, discrete implementation is provided in the study. The numerical analysis shows that our proposed method can effectively improve the energy concentration comparable to the MSST. Comparisons with other advanced methods also show that the proposed method offers better performance in addressing strongly non-stationary signals and noise-added signals. In the experimental signal analysis, we carry out three experiments to validate the effectiveness of the proposed method in the analysis of real-world signals.

© 2020 Elsevier Ltd. All rights reserved.

1. Introduction

A rotating machine with bearing defect usually produces impulse signals that can be recorded by vibration sensors [1-7]. However, vibration signal processing becomes challenging when the machine runs at variable speeds. This is because the signals measured in such situations usually exhibit strongly non-stationary characteristics, i.e., the frequency of the signal greatly changes with time. Non-stationary signal analysis has drawn increasing attention in the fault diagnosis of rotating machinery. Time-frequency (TF) analysis (TFA) technique has a powerful capacity to address such challenges. Several articles reviewing the development of TFA techniques in the fault diagnosis of rotating machinery can be found in [8-10]. It is known from recent studies that the energy concentration is a key indicator for evaluating the performance of a TFA method [11]. This is because a concentrated TF representation (TFR) has the better capacity to characterize the fault features underlying signals. However, restricted by the Heisenberg uncertainty principle, conventional TFA methods, e.g., the short time Fourier transform (STFT), wavelet transform (WT) and S transform, have difficulty providing concentrated results when addressing strongly time-varying signals. Various newly developed TFA techniques that aim at overcoming the

E-mail address: yugang2010@163.com

<https://doi.org/10.1016/j.jsv.2020.115813>

0022-460X/© 2020 Elsevier Ltd. All rights reserved.

Please cite this article as: G. Yu, A multisynchrosqueezing-based high-resolution time-frequency analysis tool for the analysis of non-stationary signals, Journal of Sound and Vibration, <https://doi.org/10.1016/j.jsv.2020.115813>

drawbacks of conventional methods have drawn amount of attention in recent decades, e.g., the reassignment method (RM) [12], synchrosqueezing transform (SST) [13,14], demodulated SST (DSST) [15,16], high-order SST [17-19], synchroextracting transform (SET) [20,21] and multi-SST (MSST) [22].

The RM technique is designed to sharpen an energy-smear TFR by mapping the data to new coordinates that are nearer to the concentrated region according to the local estimates of the instantaneous frequency (IF) and group delay of the signal [12]. Such an energy-smear TFR is usually produced by the STFT, WT or S transform in advance. However, the mapping of the RM is applied to spectrogram or scalogram that are usually defined as the squared magnitude of the STFT or WT. Such a mapping loses the phase information of the signal, which also means that the signal cannot be reconstructed from the RM result. As an RM-like post-processing technique, the SST retains the inverse ability by executing TFR mapping only according to the estimates of the IF. This makes the SST more advantageous in many fields, such as mechanical fault diagnosis [23,24], seismic signal analysis [25,26] and breathing dynamics analysis [27]. Various recent studies focus on further enhancing the capacity of the SST technique when characterizing strongly time-varying signals [13-22].

The SST technique is proposed under the framework of linear TFA algorithms, e.g., WT, STFT and S transforms. However, restricted by the drawbacks of linear TF atoms, the linear TFA methods cannot address the strongly time-varying signals very well. The corresponding TF results often suffer from the blurry energy problem. The SST also faces the same problem. The demodulated technique designs non-linear TF atoms to characterize the time-varying signal, which can effectively overcome the problems of the linear TFA method. Moreover, the novel SST methods based on the demodulated technique show promising potential for enhancing the energy concentration. Such a technique is often called DSST method [15,16]. However, the demodulated technique has to design the non-linear TF atoms based on a priori information of the signals [9]. In practice, it is hard or even impossible to determine the essential information of real-world signals in advance. This hinders the engineering applications of the DSST technique.

The high-order SST method is proposed for dealing with highly frequency-modulated (FM) signals, which does not require any information about the signals in advance [17-19]. In theory, the SST assumes that the analyzed signal should be a purely harmonic signal. This means that the SST is only suitable for addressing weakly FM signals. To improve this situation, the framework of the high-order SST is established on the more complex signal model, e.g., linear FM signals and high-order polynomial FM signals. In noise-free cases, the high-order SST can provide the highly concentrated results for strongly time-varying signals. However, recent studies have found that the high-order SST method is very sensitive to noise. It is often difficult to obtain the satisfactory results for signals with heavy noise using this method [22].

The SET method is designed to only retain the TF coefficients that are closely related to the time-varying features of the signal [20,21]. Additionally, the SET removes most of the weakly related TF coefficients. Therefore, the SET result is more concentrated than the SST result. However, the SET only provides an approximate reconstruction for the signal. The reconstructed performance decreases with increasing non-linearity of the signal.

The MSST method is introduced in a recently published paper, which employs an iterative procedure to improve the energy concentration of the SST. The MSST allows for perfect reconstruction of the signal and no requires a priori information. The study in [22] shows that the MSST can provide much more concentrated results than the RM, DSST and high-order SST when addressing both noise-free and noise-added signals. The MSST method seems to be a promising tool for achieving the ideal TFR (ITFR) [28]. However, the discussion section of [22] pointed out that a major problem appears in the MSST method, i.e. non-reassigned point problem that hinders the concentrated characterization of the TF features.

In this paper, we first provide a detailed theorem for the non-reassigned point problem in the MSST method and then present an improved MSST method that can effectively resolve this problem. This novel method still allows for perfect reconstruction for the signal and has good robustness to noise. It does not require extra parameters or a priori information on the signal and has a limited computational cost. This paper is structured as follows. The theory of the proposed method is illustrated in Section 2. The numerical and experimental validations are provided in Section 3 and Section 4, respectively. The conclusion is drawn in Section 5.

2. Improved multisynchrosqueezing transform (IMSST)

2.1. Non-reassigned point problem in the MSST

In mathematics, a time-varying signal can be modeled as

$$s(t) = A(t)e^{i\varphi(t)} \quad (1)$$

where $A(t)$ is the instantaneous amplitude, $\varphi(t)$ denotes the instantaneous phase, and its first-order derivative $\varphi'(t)$ is the IF. The MSST finds an effective way to generate a highly concentrated TFR, where the eventual target is to achieve the ITFR,

$$R(t, \omega) = A(t)\delta(\omega - \varphi'(t))e^{i\varphi(t)} \quad (2)$$

where the Dirac delta function $\delta(\cdot)$ guarantees that, the energy of the TFR can greatly concentrate on the IF trajectory. To derive the MSST method, we begin this study based on the STFT. The STFT of a function $s \in L^2(\cdot)$ with respect to the real and even window $g \in L^2(\cdot)$ is defined by

$$G(t, \omega) = \int_{-\infty}^{+\infty} g(u-t)s(u)e^{-i\omega(u-t)}du. \quad (3)$$

The STFT calculates the inner product between the signal and a series of TF atoms. Because the TF atoms are restricted by the Heisenberg uncertainty principle, the STFT only provides a blurry description for the signal. Under the assumption that the signal is weakly time-varying, i.e., $\exists \varepsilon$ is sufficiently small, $|A'(t)| \leq \varepsilon$ and $|\varphi''(t)| \leq \varepsilon$ for $\forall t$, the related STFT result of such a signal admits the following expression [22],

$$\begin{aligned} G(t, \omega) &= \int_{-\infty}^{+\infty} g(u-t)A(t)e^{i(\varphi(t)+\varphi'(t)(u-t))}e^{-i\omega(u-t)}du \\ &= A(t)e^{i\varphi(t)}\int_{-\infty}^{+\infty} g(u-t)e^{i(\varphi'(t)(u-t)-i\omega(u-t))}du \\ &= A(t)e^{i\varphi(t)}\hat{g}(\omega-\varphi'(t)) \end{aligned} \quad (4)$$

where $\hat{g}(\cdot)$ denotes the Fourier transform of the window and $\text{supp}(\hat{g}) \subset [-\Delta, \Delta]$. It is known from Eq. (4) that the energy of the STFT result smears around the IF $\omega \in [\varphi'(t) - \Delta, \varphi'(t) + \Delta]$. SST technique is developed to enhance the energy concentration of the STFT result. SST starts from the Eq. (4) to derive a two-dimensional (2D) IF estimate,

$$\begin{aligned} \hat{\omega}(t, \omega) &= \text{Re}\left(\frac{\partial_t G(t, \omega)}{iG(t, \omega)}\right) \\ &= \text{Re}\left(\frac{\partial_t (A(t)e^{i\varphi(t)}\hat{g}(\omega-\varphi'(t)))}{i(A(t)e^{i\varphi(t)}\hat{g}(\omega-\varphi'(t)))}\right) \\ &= \text{Re}\left(\frac{A(t)e^{i\varphi(t)}\hat{g}(\omega-\varphi'(t))i\varphi'(t)}{i(A(t)e^{i\varphi(t)}\hat{g}(\omega-\varphi'(t)))}\right) \\ &= \varphi'(t) \end{aligned} \quad (5)$$

where $\text{Re}(\cdot)$ denotes the real part. Eq. (5) demonstrates that $\hat{\omega}(t, \omega)$ is a good estimate for the IF of the signal. This also indicates that a reassignment operator can be employed to squeeze the blurry STFT result to a relatively concentrated region, which is written as Eq. (6).

$$Ts(t, \eta) = \int_{-\infty}^{+\infty} G(t, \omega)\delta(\eta - \hat{\omega}(t, \omega))d\omega. \quad (6)$$

Substituting Eqs. (4) and (5) into Eq. (6) to have

$$\begin{aligned} Ts(t, \eta) &= \int_{-\infty}^{+\infty} A(t)e^{i\varphi(t)}\hat{g}(\omega-\varphi'(t))\delta(\eta-\varphi'(t))d\omega \\ &= A(t)e^{i\varphi(t)}\delta(\eta-\varphi'(t))\int_{-\infty}^{+\infty} \hat{g}(\omega-\varphi'(t))d\omega \\ &= 2\pi g(0)A(t)e^{i\varphi(t)}\delta(\eta-\varphi'(t)). \end{aligned} \quad (7)$$

Compared with Eq. (4), it is clear that the SST can generate a more concentrated TFR with the help of the Dirac delta function than that of the STFT. However, many studies have shown that, the SST is very sensitive to the FM laws, which is not suitable for dealing with strongly time-varying signals. To generate a concentrated TFR for time-varying signals, the author in [22] proposed an iterative procedure to further concentrate the TFR. The iterative procedure can be written as

$$\begin{aligned} Ts^{[1]}(t, \eta) &= \int_{-\infty}^{+\infty} G(t, \omega)\delta(\eta - \hat{\omega}(t, \omega))d\omega. \\ Ts^{[2]}(t, \eta) &= \int_{-\infty}^{+\infty} Ts(t, \omega)\delta(\eta - \hat{\omega}(t, \omega))d\omega \\ Ts^{[3]}(t, \eta) &= \int_{-\infty}^{+\infty} Ts^{[2]}(t, \omega)\delta(\eta - \hat{\omega}(t, \omega))d\omega \\ &\vdots \\ Ts^{[N]}(t, \eta) &= \int_{-\infty}^{+\infty} Ts^{[N-1]}(t, \omega)\delta(\eta - \hat{\omega}(t, \omega))d\omega. \end{aligned} \quad (8)$$

It can be known from Eq. (8) that this novel method repeatedly reassigns the TFR until a satisfactory result is obtained in this iteration procedure. However, executing multiple SST operations is very time-consuming. To solve this problem, Ref. [22] further proposed to first construct a novel IF estimate $\hat{\omega}^{[N]}(t, \omega)$, where N denotes the iteration number. Then the SST operation is needed only once. This new method is named the MSST that can be expressed as Eq. (9).

$$Ts^{[N]}(t, \eta) = \int_{-\infty}^{+\infty} G(t, \omega)\delta(\eta - \hat{\omega}^{[N]}(t, \omega))d\omega. \quad (9)$$

where $\hat{\omega}^{[2]}(t, \omega) = \hat{\omega}(t, \hat{\omega}(t, \omega))$, $\hat{\omega}^{[3]}(t, \omega) = \hat{\omega}(t, \hat{\omega}(t, \hat{\omega}(t, \omega)))$, $\hat{\omega}^{[4]}(t, \omega) = \hat{\omega}(t, \hat{\omega}(t, \hat{\omega}(t, \hat{\omega}(t, \omega))))$ and so on. A numerical signal is used to illustrate the differences between the SST and MSST. This signal is modeled as Eq. (10), which is sampled by 100 Hz.

$$s(t) = \sin(2\pi(25t + 10\sin(1.5t))). \quad (10)$$

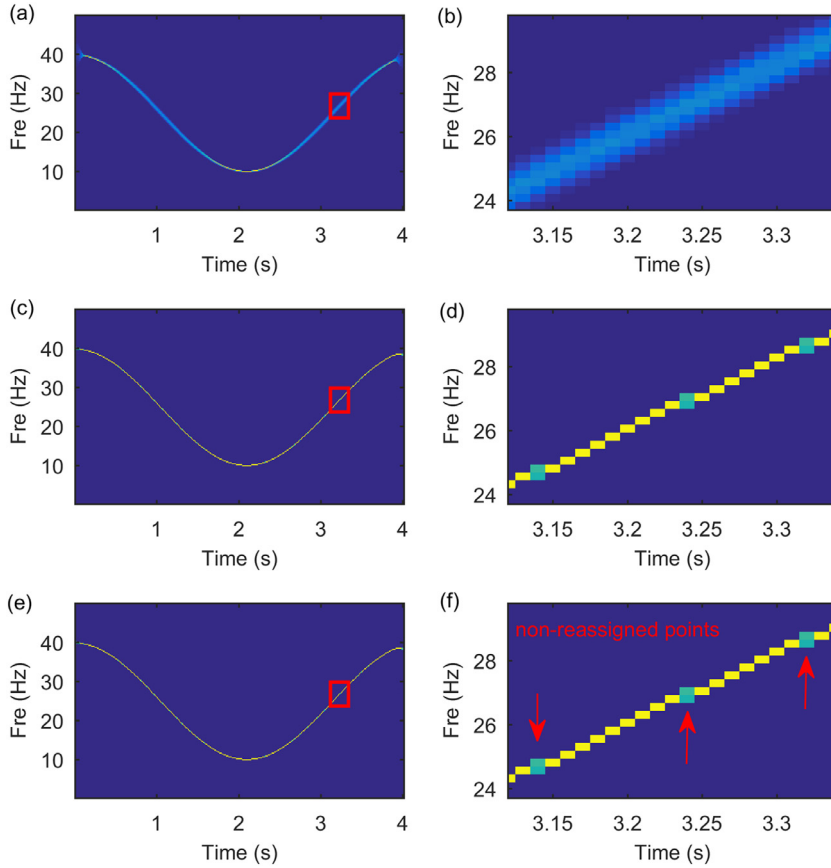


Fig. 1. (a) SFT result, (b) zoomed TF feature, (c) MSST result (N=10), (d) zoomed TF feature, (e) MSST result (N=100) and (f) zoomed TF feature, where red arrows mark the position of the non-reassigned points.

The SFT result, MSST result (N=10) and MSST result (N=100) are shown in Fig. 1. Additionally, the zoomed TF features are provided, where the zoomed part of the signal has a strongly time-varying law. Fig. 1(b) shows that the zoomed SFT result is somewhat blurry. Fig. 1(c-d) show that the MSST (N=10) effectively improves the energy concentration comparable to the SFT, where most of TF coefficients only appear in the IF. In the ideal case, all TF coefficients should be reassigned to the IF. However, the TF energy at three time points obviously spreads into two TF points around the IF during the short time of Fig. 1(d). The MSST result after one hundred iterations is displayed in Fig. 1(e-f). It can be observed that even after more iterations, the blurry TF coefficients cannot be reassigned to one TF point. This phenomenon is called the non-reassigned point problem. In Fig. 1(f), the non-reassigned points are marked via red arrows. When this problem is resolved, the MSST can provide a TFR much closer to the ITFR for strongly time-varying signals.

2.2. Improved multisynchrosqueezing (IMSST)

To explore the non-reassigned point problem of the MSST method, we first introduce a second-order time-varying signal model. We assume that $\exists \varepsilon$ is sufficiently small, $|A'(t)| < \varepsilon$, $|\varphi'''(t)| \leq \varepsilon$ for $\forall t$, which denotes that the signal given in Eq. (1) exhibits time-varying characteristics. According to the Taylor expansion, such a signal can be written as

$$s(u) = A(t)e^{i(\varphi(t) + \varphi'(t)(u-t) + 0.5\varphi''(t)(u-t)^2)}. \quad (11)$$

Moreover, we let the window function be a Gaussian function,

$$g(t) = e^{-\frac{t^2}{2\sigma}} \quad (12)$$

The Fourier transform of $g(t)$ can be calculated as

$$\hat{g}(\omega) = \sqrt{2\sigma\pi} e^{-\frac{\sigma\omega^2}{2}} \quad (13)$$

We then substitute Eq. (11) and Eq. (12) into Eq. (3) and the STFT of the signal given in Eq. (11) can be derived as

$$\begin{aligned} G(t, \omega) &= \int_{-\infty}^{+\infty} e^{-\frac{(u-t)^2}{2\sigma^2}} A(t) e^{i(\varphi(t)+\varphi'(t)(u-t)+0.5\varphi''(t)(u-t)^2)} e^{-i\omega(u-t)} du \\ &= A(t) e^{i\varphi(t)} \int_{-\infty}^{+\infty} e^{-(2\sigma)^{-1}(1-i\sigma\varphi''(t))(u-t)^2} e^{-i(\omega-\varphi'(t))(u-t)} d(u-t) \\ &= A(t) e^{i\varphi(t)} \sqrt{\frac{2\sigma\pi}{1-i\sigma\varphi''(t)}} e^{-\frac{\sigma(\omega-\varphi'(t))^2}{2-2i\sigma\varphi''(t)}}. \end{aligned} \quad (14)$$

For this time-varying signal model, according to Eq. (5), we can also derive that,

$$\hat{\omega}(t, \omega) = \varphi'(t) + \frac{\varphi''(t)^2}{1/\sigma^2 + \varphi''(t)^2} (\omega - \varphi'(t)). \quad (15)$$

Moreover, the IF estimate $\hat{\omega}^{[N]}(t, \omega)$ after N iterations can be expressed as

$$\hat{\omega}^{[N]}(t, \omega) = \varphi'(t) + \left(\frac{\varphi''(t)^2}{1/\sigma^2 + \varphi''(t)^2} \right)^N (\omega - \varphi'(t)). \quad (16)$$

After N iterations, the error between $\hat{\omega}^{[N-1]}(t, \omega)$ and $\hat{\omega}^{[N]}(t, \omega)$ will decrease with increasing iteration number as expressed in Eq. (17).

$$\lim_{N \rightarrow \infty} |\hat{\omega}^{[N]}(t, \omega) - \hat{\omega}^{[N-1]}(t, \omega)| = \lim_{N \rightarrow \infty} \left| \left(\frac{\varphi''(t)^2}{1/\sigma^2 + \varphi''(t)^2} \right)^{N-1} \frac{\omega - \varphi'(t)}{1 + \sigma^2 \varphi''(t)^2} \right| = 0. \quad (17)$$

Thus, we can stop the iterative procedure when the condition given in Eq. (18) is satisfied.

$$\int_{-\infty}^{+\infty} \int_{-\infty}^{+\infty} |\hat{\omega}^{[N]}(t, \omega) - \hat{\omega}^{[N-1]}(t, \omega)| dt d\omega < \lambda \quad (18)$$

where λ is a small threshold.

It is known from Eq. (16) that regardless of how many iterations we execute, $\hat{\omega}^{[N]}(t, \omega)$ is always a biased estimate for the IF of the signal. In theory, the MSST method reassigns the TF coefficients $G(t, \omega)|_{\omega \in [\varphi'(t)-\Delta, \varphi'(t)+\Delta]}$ to the position $(t, \hat{\omega}^{[N]}(t, \omega))$. In discrete signal processing, before executing the reassigning operation, the parameter $\hat{\omega}^{[N]}(t, \omega)$ has to be rounded to the nearest integer. The rounding operation can be found in Eq. (19).

$$\text{Round}(x) = \begin{cases} [x] & , \text{ if } x < [x] + 0.5 \\ [x + 1] & , \text{ if } x \geq [x] + 0.5 \end{cases} \quad (19)$$

where $[x]$ is the integer part of x .

In most cases, the $\hat{\omega}^{[N]}(t, \omega)$ after the rounding operation will be rounded to the same integer nearest to the IF. Thus, the blurry TF coefficients can be reassigned to a concentrated region. However, in some special cases, $\hat{\omega}^{[N]}(t, \omega)$ may be rounded to two adjacent integers, which leads to the non-reassigned point problem. We suppose that at the time instant t_0 , the IF of the signal is $\varphi'(t_0) = Z_0 + 0.5$, where Z_0 denotes the integer. According to Eq. (16), we obtain that,

$$\hat{\omega}^{[N]}(t_0, \omega) = Z_0 + 0.5 + \left(\frac{\varphi''(t_0)^2}{1 + \varphi''(t_0)^2} \right)^N (\omega - \varphi'(t_0)). \quad (20)$$

Because that,

$$\lim_{N \rightarrow \infty} \left(\frac{\varphi''(t_0)^2}{1 + \varphi''(t_0)^2} \right)^N = 0. \quad (21)$$

Hence, it can be assumed that after enough iteration, $\exists \varepsilon$ is sufficiently small for $\omega \in [\varphi'(t_0) - \Delta, \varphi'(t_0) + \Delta]$, we have

$$\left| \left(\frac{\varphi''(t_0)^2}{1 + \varphi''(t_0)^2} \right)^N (\omega - \varphi'(t_0)) \right| < \varepsilon. \quad (22)$$

Therefore, the parameter $\hat{\omega}^{[N]}(t_0, \omega)$ after the rounding operation should be

$$\text{Round}(\hat{\omega}^{[N]}(t_0, \omega)) = \begin{cases} Z_0, & \text{if } \omega < \varphi'(t_0) \\ Z_0 + 1, & \text{if } \omega \geq \varphi'(t_0) \end{cases} \quad (23)$$

It is known from Eq. (23) that when the IF of the signal is $\varphi'(t_0) = Z_0 + 0.5$, the TF coefficients $G(t_0, \omega)|_{\omega \in [\varphi'(t_0)-\Delta, \varphi'(t_0)]}$ and $G(t_0, \omega)|_{\omega \in [\varphi'(t_0), \varphi'(t_0)+\Delta]}$ have to be reassigned to two frequency points Z_0 and $Z_0 + 1$, which

finally leads to the non-reassigned point problem. To solve this problem, we deal with the IF estimate $\hat{\omega}^{[N]}(t, \omega)$ via two rounding operations,

$$\hat{\omega}_R^{[N]}(t, \omega) = \text{Round}(\text{Round}(2\hat{\omega}^{[N]}(t, \omega))/2). \quad (24)$$

If $(\frac{\varphi''(t_0)^2}{1+\varphi''(t_0)^2})^N (\omega - \varphi'(t_0)) < 0.25$, we can obtain

$$\hat{\omega}_R^{[N]}(t_0, \omega) = Z_0 + 1, \text{ for } \omega \in [\varphi'(t_0) - \Delta, \varphi'(t_0) + \Delta]. \quad (25)$$

Eq. (25) denotes that via two rounding processes, the TF coefficients $G(t_0, \omega)|_{\omega \in [\varphi'(t_0) - \Delta, \varphi'(t_0)]}$ and $G(t_0, \omega)|_{\omega \in [\varphi'(t_0), \varphi'(t_0) + \Delta]}$ can be reassigned to one frequency point $Z_0 + 1$, which can effectively address the blurry energy problem of the MSST. Actually, we can execute enough iterations to guarantee that the Eq. (26) is satisfied.

$$\left(\frac{\varphi''(t)^2}{1 + \varphi''(t)^2} \right)^N (\omega - \varphi'(t)) < 0.25. \quad (26)$$

Therefore, the non-reassigned point problem in the original MSST algorithm can be resolved well. The related expression should be rewritten as

$$Ts^{[N]}(t, \eta) = \int_{-\infty}^{+\infty} G(t, \omega) \delta(\eta - \hat{\omega}_R^{[N]}(t, \omega)) d\omega. \quad (27)$$

To distinguish it from the MSST, Eq. (27) is named the improved MSST (IMSST). The following expressions show that the original signal can be perfectly reconstructed from the IMSST result,

$$\begin{aligned} & \int_{-\infty}^{+\infty} Ts^{[N]}(t, \eta) d\eta \\ &= \int_{-\infty}^{+\infty} \int_{-\infty}^{+\infty} G(t, \omega) \delta(\eta - \hat{\omega}_R^{[N]}(t, \omega)) d\omega d\eta \\ &= \int_{-\infty}^{+\infty} G(t, \omega) \int_{-\infty}^{+\infty} \delta(\eta - \hat{\omega}_R^{[N]}(t, \omega)) d\eta d\omega \\ &= \int_{-\infty}^{+\infty} G(t, \omega) d\omega \\ &= (2\pi g(0))s(t). \end{aligned} \quad (28)$$

Thus,

$$s(t) = (2\pi g(0))^{-1} \int_{-\infty}^{+\infty} Ts^{[N]}(t, \omega) d\omega. \quad (29)$$

2.3. Discrete implementation of IMSST

In this section, we consider the discrete implementation of the IMSST. To obtain the parameter $\hat{\omega}(t, \omega)$, we first have

$$\begin{aligned} \partial_t G(t, \omega) &= \partial_t \left(\int_{-\infty}^{+\infty} g(u-t)s(u)e^{-i\omega(u-t)} du \right) \\ &= - \int_{-\infty}^{+\infty} g'(u-t)s(u)e^{-i\omega(u-t)} du + i\omega \cdot \int_{-\infty}^{+\infty} g(u-t)s(u)e^{-i\omega(u-t)} du \\ &= -G^g(t, \omega) + i\omega G(t, \omega) \end{aligned} \quad (30)$$

Thus, a 2D IF estimate can be calculated by

$$\hat{\omega}(t, \omega) = \text{Re} \left(\omega + i \frac{G^g(t, \omega)}{G(t, \omega)} \right). \quad (31)$$

Given the discrete data $s[l]$, $n = 0, 1, \dots, L-1$, where L is the number of samples and the data $s[l]$ correspond to a uniform discretization of $s(t)$ taken at time $t_n = t_0 + lT$, in which T is the sampling interval. The Fourier transform of the data $s[l]$ is calculated by $S[m] = \sum_{l=0}^{L-1} s[l]e^{-i\frac{2\pi}{L}lm}$, where $l = 0, 1, \dots, L-1$. From Eq. (31), it is known that, the IMSST algorithm needs to calculate two STFTs ($G[h, m]$ and $G^g[h, m]$) with respect to windows $g[h]$ and $g'[h]$. The corresponding expressions are written as Eq. (32) and Eq. (33), respectively.

$$G[h, m] = \sum_{l=0}^{L-1} s[l]g[l-h]e^{-i\frac{2\pi}{L}[l-h]m}. \quad (32)$$

$$G^g[h, m] = \sum_{l=0}^{L-1} s[l]g'[l-h]e^{-i\frac{2\pi}{L}[l-h]m}. \quad (33)$$

Algorithm 1 Discrete implementation of IMSST.**Step 1 : Initialization**

Choose the window function g and iteration number N ;

Step 2 : Calculation

$$G[h, m] \leftarrow \sum_{l=0}^{L-1} s[l] g[l-h] e^{-i\frac{2\pi}{L}(l-h)m}; G^g[h, m] \leftarrow \sum_{l=0}^{L-1} s[l] g^g[l-h] e^{-i\frac{2\pi}{L}(l-h)m};$$

$$\hat{\omega}[t, \omega] \leftarrow m + \operatorname{Re} \left(\frac{iG^g[h, m]}{G[h, m]} \right);$$

Step 3 : Iteratively Construct novel IF estimate

$$\hat{\omega}^{[1]}[h, m] \leftarrow \hat{\omega}[h, m];$$

if $N > 1$

 for $n = 2 : N$

 for $h = 1 : L$

 for $m = 1 : L$

$$\xi \leftarrow \operatorname{Round}(\hat{\omega}^{[n-1]}[h, m]);$$

$$\hat{\omega}^{[n]}[h, m] \leftarrow \hat{\omega}^{[n-1]}[h, \xi];$$

 end for

 end for

 end for

end if

Step 4 : Rounding IF estimate

$$\hat{\omega}_r^{[N]}[h, m] = \operatorname{Round}(\operatorname{Round}(2\hat{\omega}^{[N]}[h, m]) / 2);$$

Step 5 : Synchrosqueezing

$$T_s^{[N]}[h, \xi] \leftarrow 0;$$

for $h = 1 : L$

 for $m = 1 : L$

$$\xi \leftarrow \hat{\omega}_r^{[N]}[h, m];$$

$$T_s^{[N]}[h, \xi] \leftarrow T_s^{[N]}[h, \xi] + G[h, m];$$

 end for

end for

output $T_s^{[N]}[h, \xi];$

Then the discrete 2D IF estimate $\hat{\omega}[h, m]$ can be written as

$$\hat{\omega}[t, \omega] = m + \operatorname{Re} \left(\frac{iG^g[h, m]}{G[h, m]} \right). \quad (34)$$

The entire pseudocode of the IMSST can be found in [Algorithm 1](#), where ξ denotes the discrete frequency variable. Moreover, the discrete signal reconstruction expression can be written as

$$s[h] = (2\pi g(0))^{-1} \sum_{m=0}^{L-1} T_s^{[N]}[h, m]. \quad (35)$$

Algorithm 1 mainly includes four steps and only executes the SST operation once in the last step. Therefore, the IMSST method should have the same computational burden level as the SST method. The TFR of the signal given in [Eq. \(10\)](#) generated by the IMSST is shown in [Fig. 2\(a\)](#), and the zoomed TF feature follows in [Fig. 2\(b\)](#). It can be clearly observed that all TF coefficients are reassigned to one TF point and the TFR only appears in the IF trajectory. Furthermore, we reconstruct this numerical signal via the IMSST result and plot it in [Fig. 2\(c\)](#) compared to the original signal. It can be seen that the reconstructed signal is highly consistent with the original signal, which validates the perfectly revertible nature of the IMSST.

To quantitatively support the superiority of the IMSST over the MSST in concentrating the TF energy, we calculate the Rényi entropies of the TF results generated by these two methods with respect to the iteration number, where a lower Rényi entropy value denotes a more concentrated TFR. The calculated results are displayed in [Fig. 3](#). It can be observed that both the MSST and IMSST have fast energy-concentration speeds. After six iterations, the Rényi entropy tends to be stable. However, due to the existence of the non-reassigned points, the MSST result is blurrier than the IMSST result after three iterations. This comparison validates the effectiveness of the IMSST in concentrating TF energy.

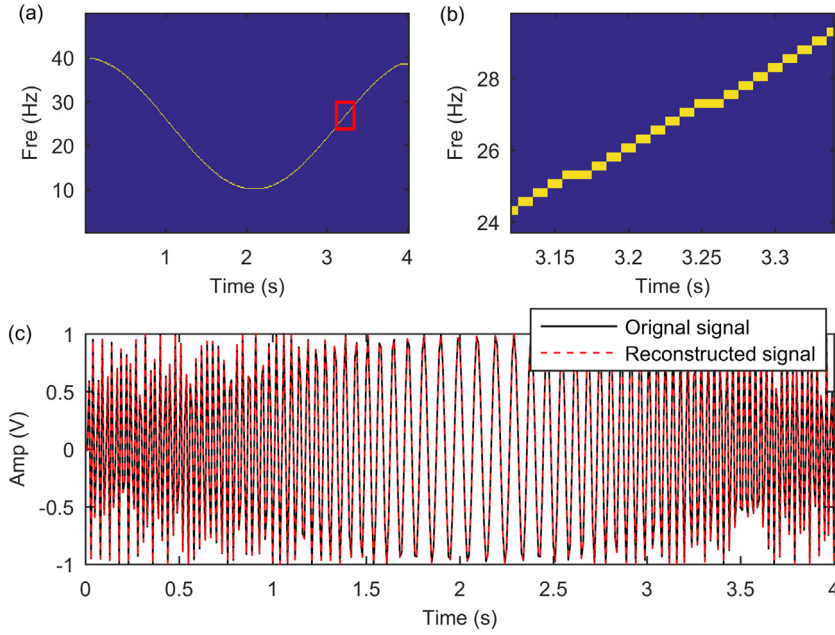


Fig. 2. (a) IMSST result, (b) zoomed TF feature and (c) the reconstructed signal comparing with the original signal.

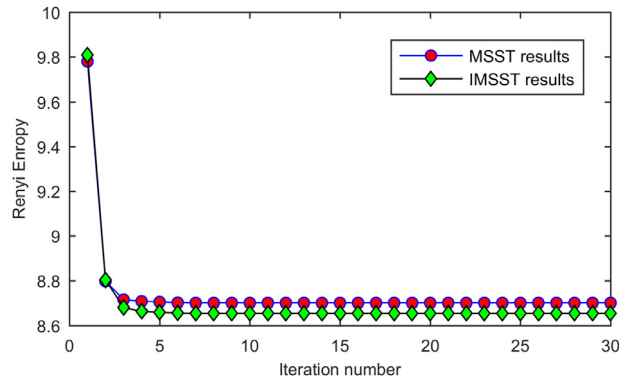


Fig. 3. Rényi entropies of the TFRs generated by the MSST and IMSST.

3. Numerical signal analysis

In this section, we focus on the comparisons between the proposed method and other advanced TFA methods in addressing complex signals, for instance, noise-added signals and time-varying multi-component signals. The comparisons mainly focus on the TF energy concentration, TF resolution and signal reconstruction.

3.1. Noisy signal analysis

In this section, we mainly test the performance of the proposed method in addressing noise-added signals. Hence, white noise is added to the signal given in Eq. (10) where the signal to noise ratio (SNR) is equal to 5 dB. In Fig. 4, we first list the TFRs generated by the MSST and IMSST. In Fig. 4(b), it can be seen that the MSST result for this signal has more non-reassigned points than the MSST result for the noise-free signal in this zoomed plane. This means that the noise can also damage the energy concentration of the MSST result. However, in Fig. 4(d), it is obvious that the IMSST still provides a more concentrated result for the noise-added signal.

For more comparisons, the TFRs generated by the SST, second-order SST, fourth-order SST and SET methods are shown in Fig. 5. It can be observed that the SST result is too blurry to clearly characterize this signal. Although the high-order SST results are relatively concentrated, the noise still heavily affects the TFR. The SET result seems to be more concentrated. The

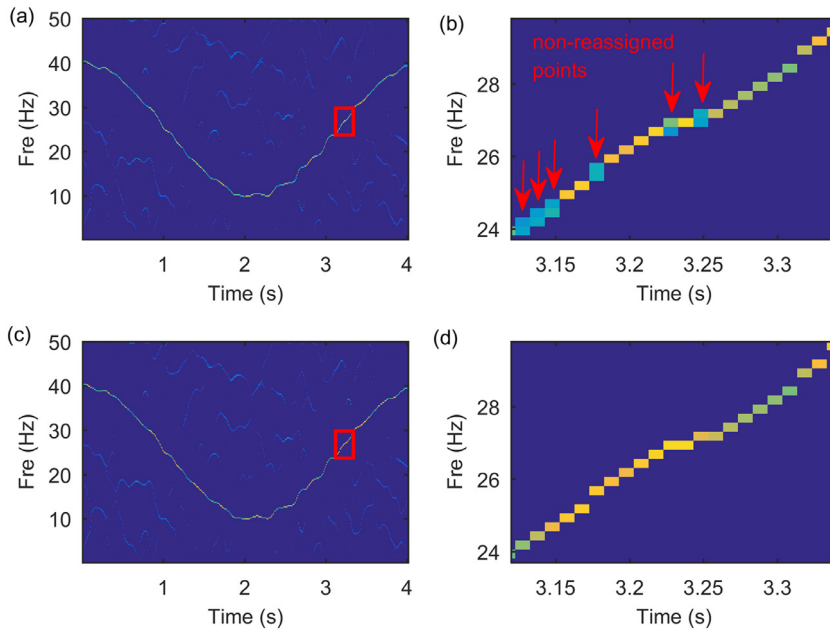


Fig. 4. (a) MSST result, (b) zoomed TF feature, (c) IMSST result, (d) zoomed TF feature.

TF slices are then used to compare the performances of different methods. The better ability of the reassigned techniques to concentrate the TF coefficients should generate a TFR with a narrower energy distribution and larger TF amplitude. The TF slices at 3.21 s and 3.23 s are plotted in Fig. 6. Because there are no non-reassigned points in the MSST result at 3.21 s, the MSST and IMSST results have the same energy distribution and the same TF amplitude in Fig. 6(a). However, because there exists a non-reassigned point in the MSST result at 3.23 s as shown in Fig. 6(b), the IMSST result appears to be more concentrated than the MSST result. It can also be seen that in these two TF slices, the other TFA results exhibit much wider energy distribution and lower TF amplitude than the IMSST result.

To more comprehensively test the performance of the proposed method, we add more noise under different SNR levels to the signal given in Eq. (10), where the SNR ranges from 1 dB to 30 dB. The Rényi entropies of the different TFA methods used to address these noisy signals are listed in Fig. 7. It is shown that the high-order SST results have lower Rényi entropies than the SST results but have larger Rényi entropies than the SET results. The MSST method generates TFRs with Rényi entropies lower than these methods. After addressing the non-reassigned point problem, the IMSST method further improves the energy concentration of the TFRs for these noise-added signals under each SNR level.

For more comparisons, the IF curves characterized by various TFA techniques are estimated using the ridge detection algorithm, which are evaluated by the relative error (RE) with the true IF given in Eq. (36).

$$RE = \frac{\|IF(t) - IF_e(t)\|_2}{\|IF(t)\|_2} \quad (36)$$

where $\|\cdot\|_2$ indicates the L2 norm, $IF(t)$ is the true IF curve of the signal and $IF_e(t)$ denotes the estimated IF of the signal. Fig. 8 shows the relative errors between the estimated IF and the true IF under various SNR levels. It is shown that the IF characterized by the IMSST technique has the smallest error in most cases. Fig. 9 shows the estimated IFs generated by the high-order SST and IMSST. The zoomed features show that the precise estimation of the IF from the IMSST result benefits from the energy-concentrated TFR. The smeared TF energy of the high-order SST leads to an unstable estimation in the analysis of the noise-added signals.

The reconstruction performances of the MSST and IMSST methods are compared under each SNR level. For these two methods, the TF coefficient in the IF trajectory is used to reconstruct the signal. The SNRs of the reconstructed signals by these two methods are listed in Fig. 10. It is shown that, from 1 dB to 6 dB, these two methods provide similar reconstruction for the signal. In other cases, the IMSST reconstructs the signals with larger SNR than the MSST. In Fig. 11, we give the recovered signals by two methods, where the SNR is 15 dB. The amplitude of the signal reconstructed from the MSST result is obviously less than the original signal at the time instant marked by the red arrow as shown in Fig. 11(a), while the IMSST provides a more satisfactory result. It can be concluded that, at low SNR level, the noise has the key effect on the reconstructed results of the two methods. At high SNR level, the non-reassigned point problem becomes the key restriction on the reconstruction performance of the MSST method.

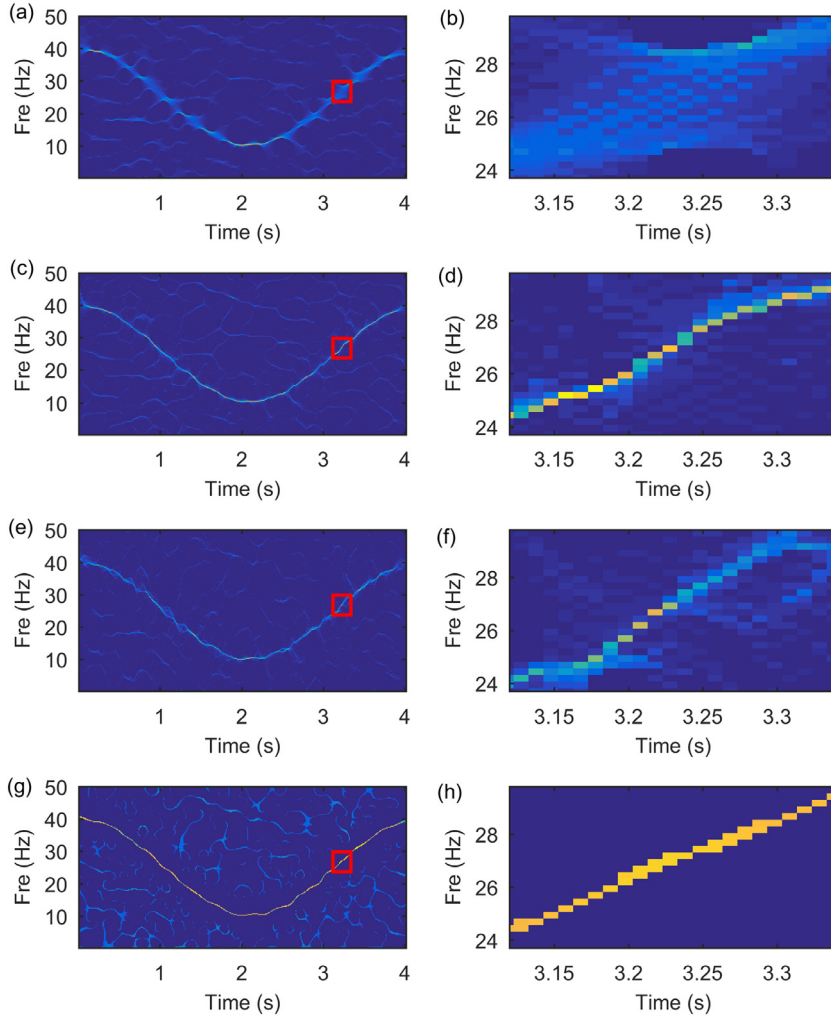


Fig. 5. (a) SST result, (b) zoomed TF feature, (c) second-order SST result, (d) zoomed TF feature, (e) forth-order SST result, (f) zoomed TF feature, (g) SET result and (h) zoomed TF feature.

3.2. Strongly time-varying signal analysis

A strongly time-varying signal is analyzed in this section, which is modeled as Eq. (37).

$$S(t) = \underbrace{\sin(2\pi(340t - 2 \exp(-2t + 0.4) \sin(14\pi(t - 0.2))))}_{S_1} + \underbrace{\sin(2\pi(75t + 30t^3))}_{S_2} \quad (37)$$

where component S_1 is strongly time-varying and component S_2 is weakly time-varying. Fig. 12 shows the TFRs generated by the fourth-order SST, MSST and IMSST methods. Additionally, the zoomed TF features of component S_1 follow on the right side. It can be observed that the MSST result is more concentrated than the high-order SST result. However, the non-reassigned points that appear in the MSST result affect the characterization of the TF features. The IMSST provides a highly concentrated result for this strongly time-varying signal. S_1 and S_2 are reconstructed via the TF coefficient only in the IF from these three TFRs as shown in Fig. 13. All three methods reconstruct the weakly time-varying component S_2 very well. However, for component S_1 , the more concentrated TF result provides the reconstructed result that is much closer to the original signal.

3.3. Frequency-modulated signals analysis

A series of frequency-modulated (FM) signals with various FM rates are constructed to test the performance of the proposed technique. Such signals are modeled as Eq. (38).

$$S(t) = \cos(0.4(t - 1)) \sin(2\pi(5t + ct^2)), \quad c = 0.1, 0.2, \dots, 5, \quad 0 \leq t \leq 4 \quad (38)$$

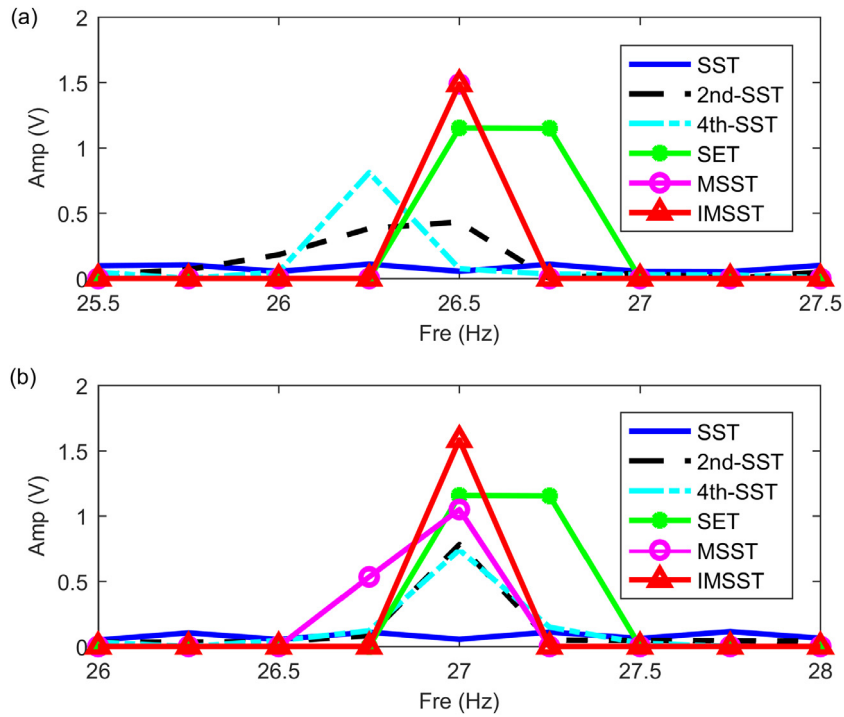


Fig. 6. TF slices of different TF results at (a) 3.21 s and (b) 3.23 s.

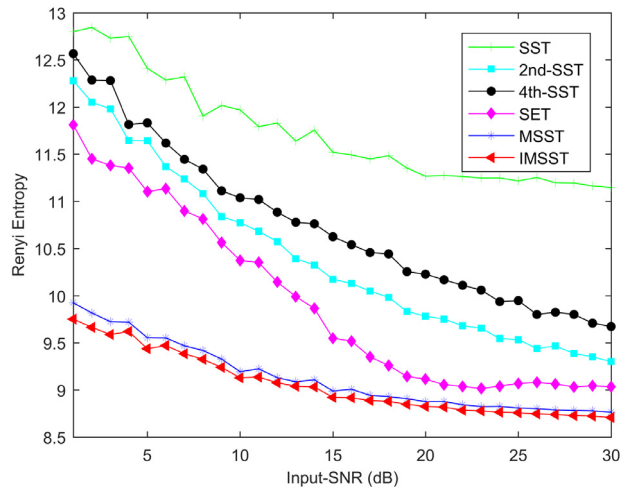


Fig. 7. Rényi entropies of the TFRs generated by different methods.

The Rényi entropy is used to evaluate the energy concentration of the IMSST and MSST results under various FM rates as shown in Fig. 14. It is observed that the Rényi entropies of the MSST results increase with increasing FM rates, while the IMSST results appear to have lower values. Moreover, Fig. 15 shows the TFRs generated from the MSST and IMSST methods when $c=5$. The zoomed TF features show that there are no non-reassigned points appeared in the IMSST result. This further confirms the capacity of the IMSST technique to address such signals.

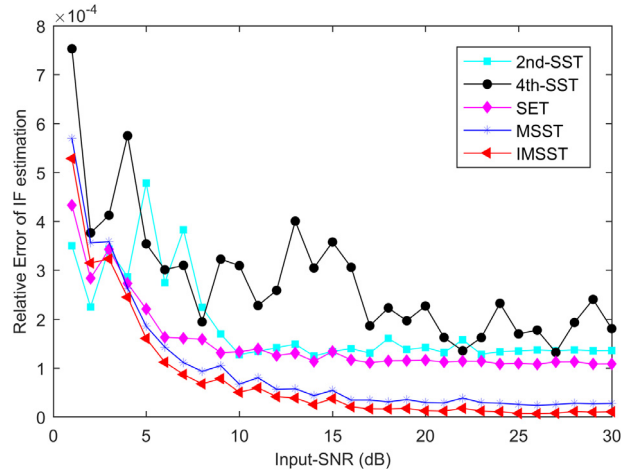


Fig. 8. The relative errors of the IF estimated by various TFA methods.

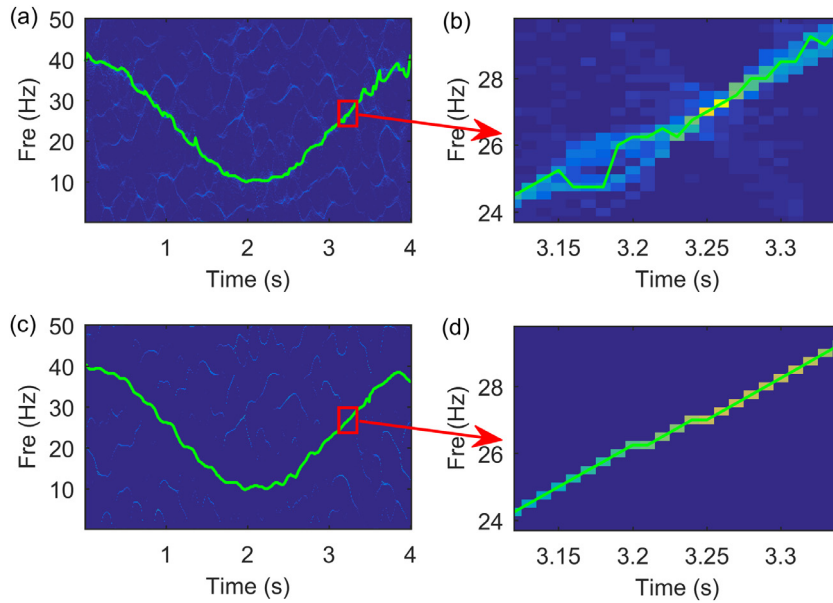


Fig. 9. (a) IF estimated from high-order SST result, (b) zoomed features, (c) IF estimated from IMSST result and (d) zoomed features.

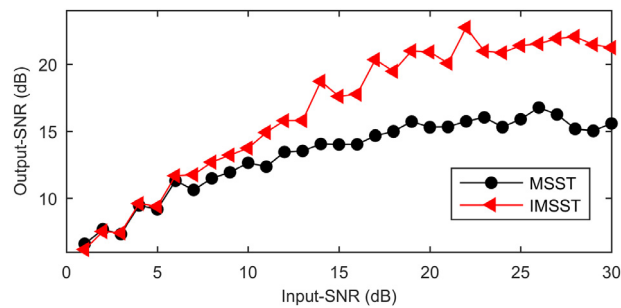


Fig. 10. Reconstruction performances of the MSST and IMSST.

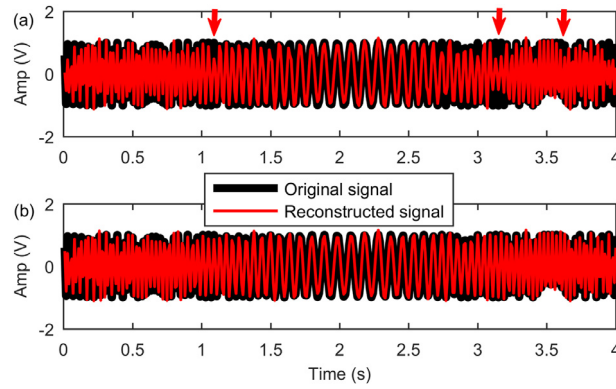


Fig. 11. Reconstructed signals by (a) MSST and (b) IMSST.

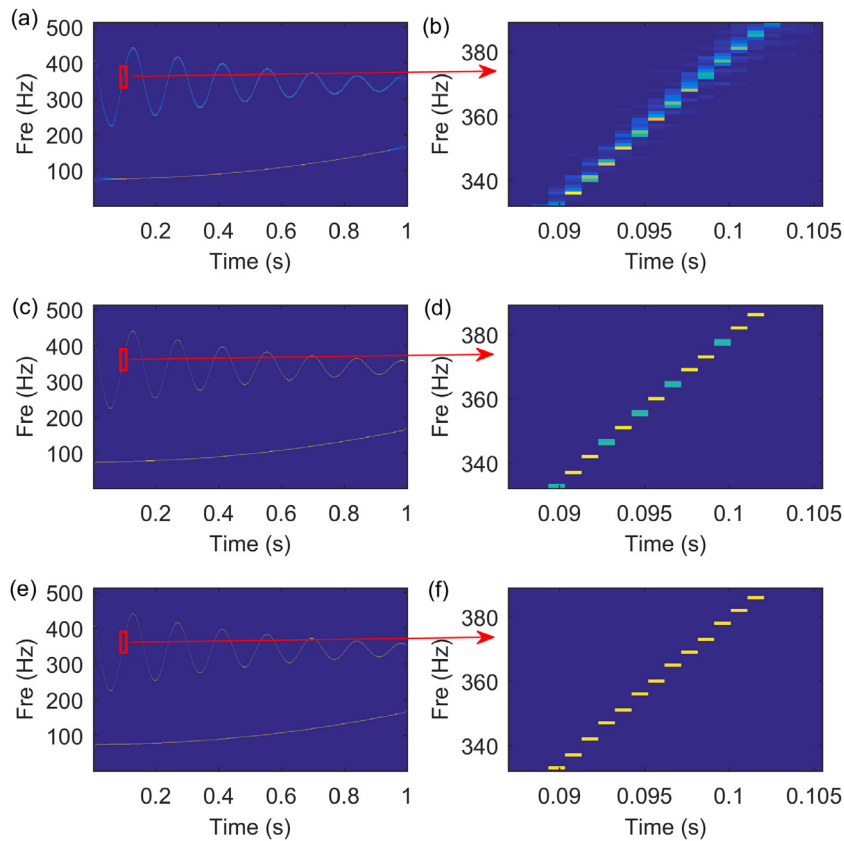


Fig. 12. (a) Fourth-order SST result, (b) zoomed TF feature, (c) MSST result, (d) zoomed TF feature, (e) IMSST result and (f) zoomed TF feature.

4. Experimental signal analysis

In this section, we mainly test the ability of the proposed IMSST method to deal with several experimental signals, which include a bat signal, a vibration signal of a rotating machine with a rub impact fault and two vibration signals of a rotating machine with an outer race fault and inner race fault under variable speed conditions.

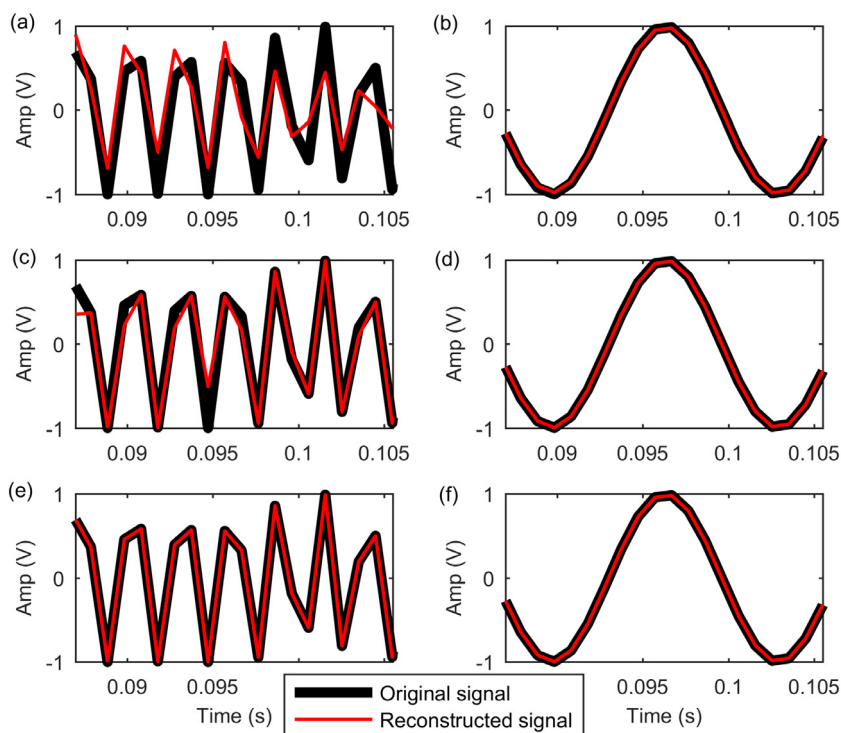


Fig. 13. (a) S1 and (b) S2 reconstructed by forth-order SST, (c) S1 and (d) S2 reconstructed by MSST, (e) S1 and (f) S2 reconstructed by IMSST.

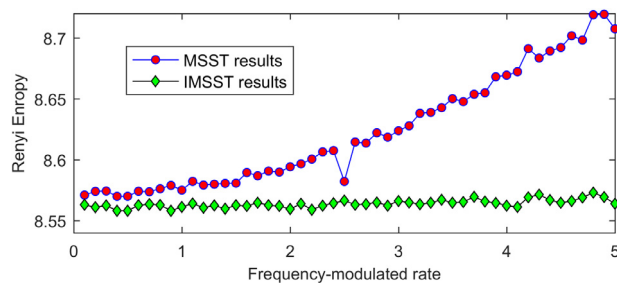


Fig. 14. Rényi entropies of the TFRs generated by the MSST and IMSST.

4.1. Bat signal

A bat signal was recorded by Rice University that was sampled at 400 points at a sampling frequency of 140 kHz, where the waveform and spectrum are displayed in Fig. 16 [29,30]. It is a multi-component signal with typical FM laws. Fig. 17(a) and (c) show the TFRs generated by the MSST and IMSST methods. Although these two TFRs seem to be very similar, in Fig. 17(b) and (d), the zoomed features show that the MSST result greatly suffers from the non-reassigned point problem. In this short time, three non-reassigned points affect the characterization of the TF features. From the smeared MSST result, it is hard to determine more precise instantaneous information, e.g., the instantaneous amplitude and IF. The IMSST provides a highly concentrated result as shown in Fig. 17(d). It can be observed that only one TF coefficient appears to represent the time-varying features of the bat signal at each time instant. From the concentrated IMSST result, it is possible to determine the precise information for each time instant. For comparisons, Fig. 18 shows the TFRs generated by the SST and RM. It is seen that the energy of these two TFRs is obviously blurry compared to the IMSST result.

To decompose this signal into multiple components, the ridge detection method in [31] is first employed to estimate the IF trajectories. Fig. 19(a) shows that there are four trajectories estimated from the TFR. The TF coefficients in the IF trajectory are used to recover each component as shown in Fig. 19(b-e). The superposition of the four components is plotted together

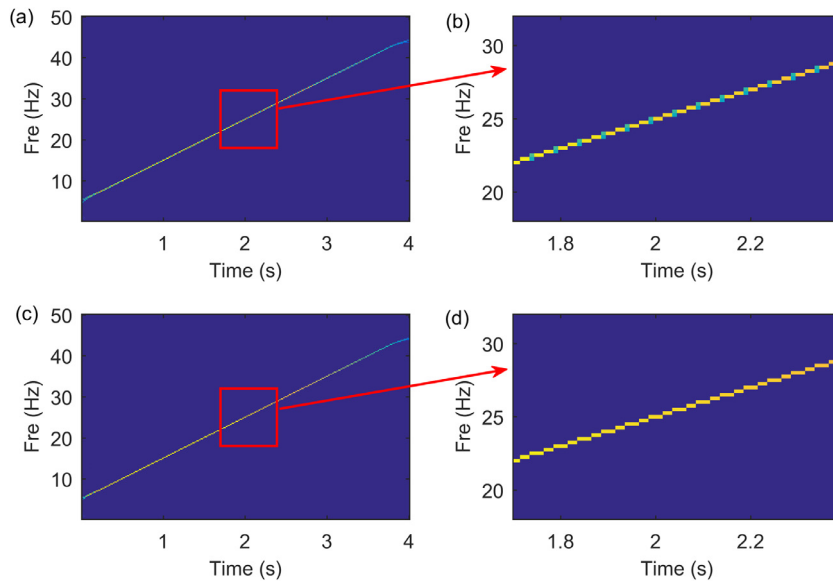


Fig. 15. (a) MSST result, (b) zoomed TF feature, (c) IMSST result and (d) zoomed TF feature.

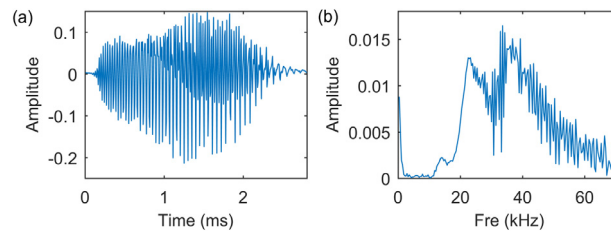


Fig. 16. (a) Waveform of the bat signal and (b) its spectrum.

with the original bat signal as shown in Fig. 19(f). It is seen that the sum of the reconstructed component is highly consistent with the original signal, which illustrates the reversibility of the IMSST method.

4.2. Vibration signal of a rotating machine with run impact fault

Rotor systems can be widely found in industrial fields [32,33]. Discovering underlying faults as early as possible is a highly challenging task for machinery condition monitoring. Rub impact often occurs as an early fault in a rotor system, which is caused by the impact between the rotor and stator element [34,35]. The rub impact fault of a rotating machine is analyzed in this section [36]. The structural sketch of the machine set is shown in Fig. 20. The rub impact is produced by tightening the screw above the rotor. The vibration of the rotor is measured by the displacement sensor, where the sampling frequency is 2560 Hz and the sampling time is 0.4 s. Additionally, the rotating speed is 5057 rpm, where the rotating frequency approximates to 84.3 Hz. The waveform and spectrum of the vibration signal are plotted in Fig. 21. The main component lies at 85 Hz, which is equal to the rotating frequency.

The TFR generated by the IMSST is shown in Fig. 22(a). There are four components that are clearly characterized, which are marked by C1, C2, C3 and C4. It can be observed that each component appears to periodically oscillate. To extract the oscillation features, the ridge detection algorithm is used to estimate the IF trajectories of four components, which are plotted in Fig. 22(b). The frequency spectrum of the IF trajectories of these four components are calculated as shown in Fig. 23. It is seen that the components C1 and C2 tend to harmonically oscillate and have the same oscillation frequency as the rotating frequency. Although 85 Hz is the main oscillation mode of components C3 and C4, they appear to be more irregular than that of C1 and C2.

Furthermore, the waveforms of the four components from the IMSST result are reconstructed as shown in Fig. 24. Component C1 has the largest amplitude, the C2 tends to be weakly amplitude-modulated (AM). For the high frequency components C3 and C4, although they have weak amplitudes, more obvious AM features appear in their waveforms, which

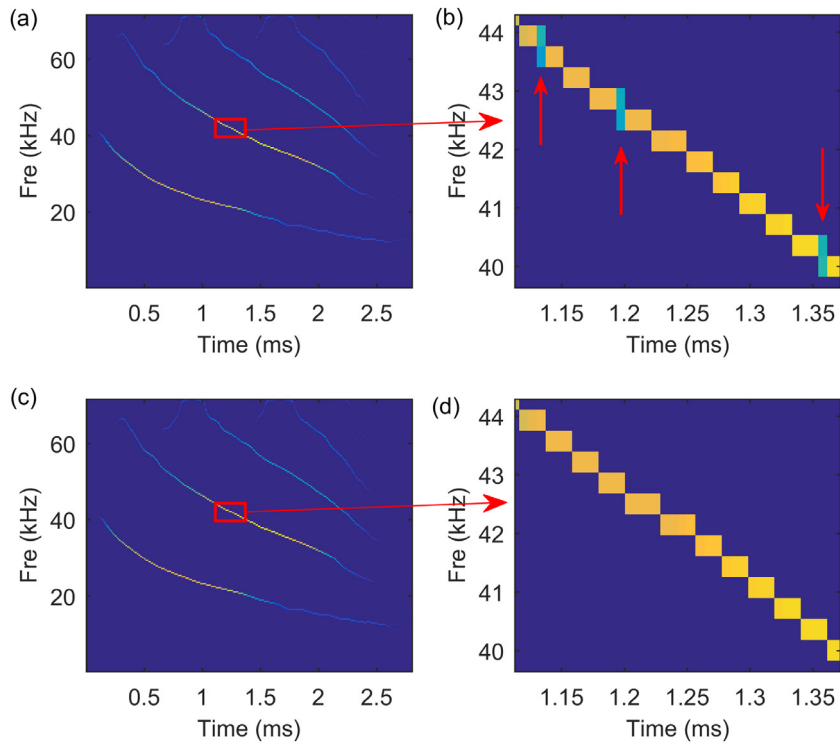


Fig. 17. (a) MSST result, (b) zoomed MSST result, (c) IMSST result and (d) zoomed IMSST result.

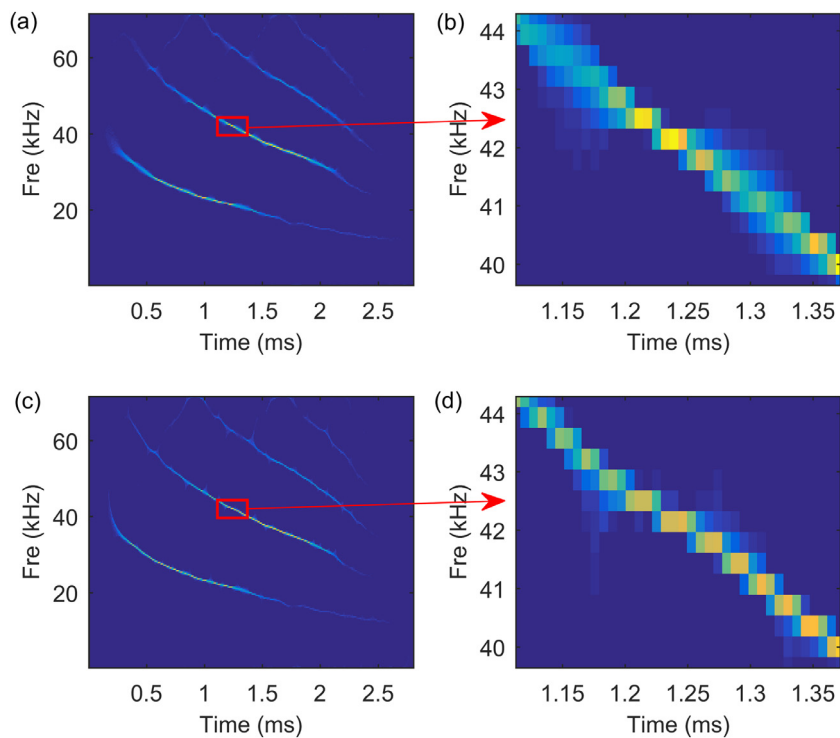


Fig. 18. (a) SST result, (b) zoomed SST result, (c) RM result and (d) zoomed RM result.

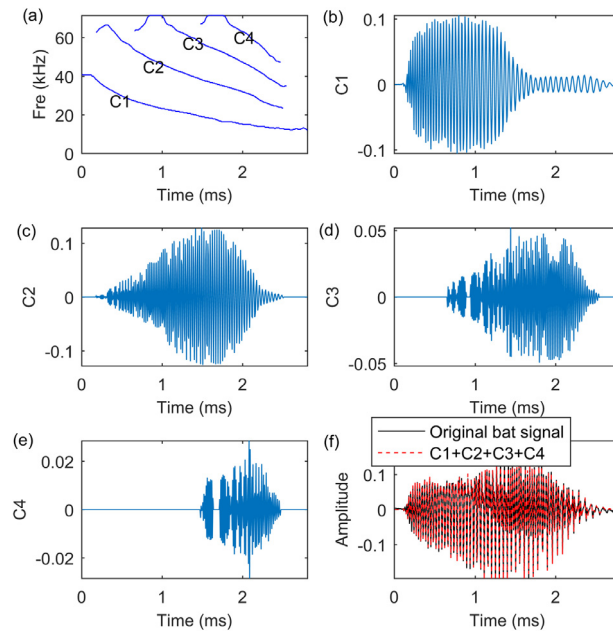


Fig. 19. (a) IF trajectories of four components, (b) C1, (c) C2, (d) C3, (e) C4 and (f) sum of four components.

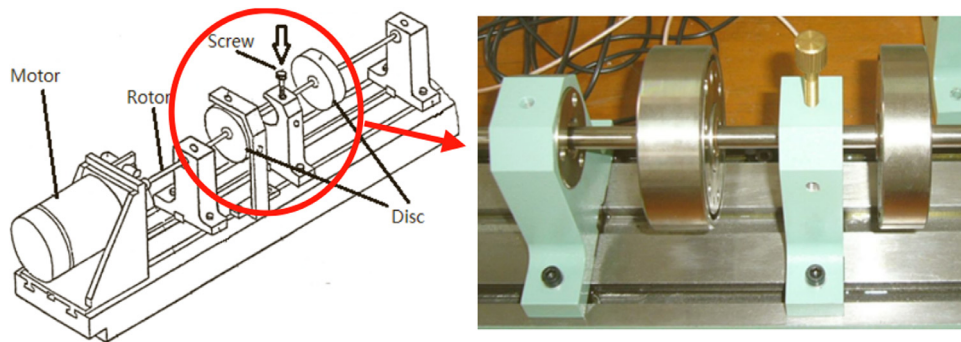


Fig. 20. Structural sketch of the machine set.

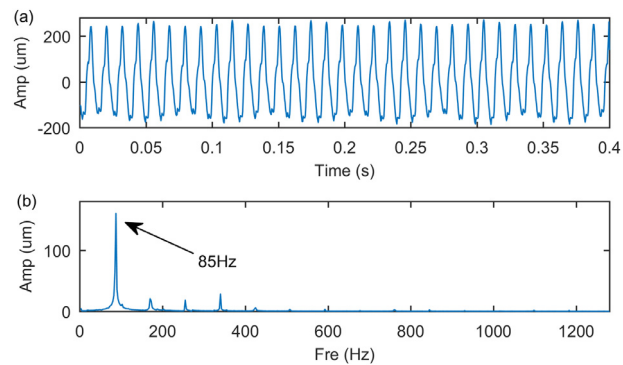


Fig. 21. (a) Waveform of vibration signal and (b) its spectrum.

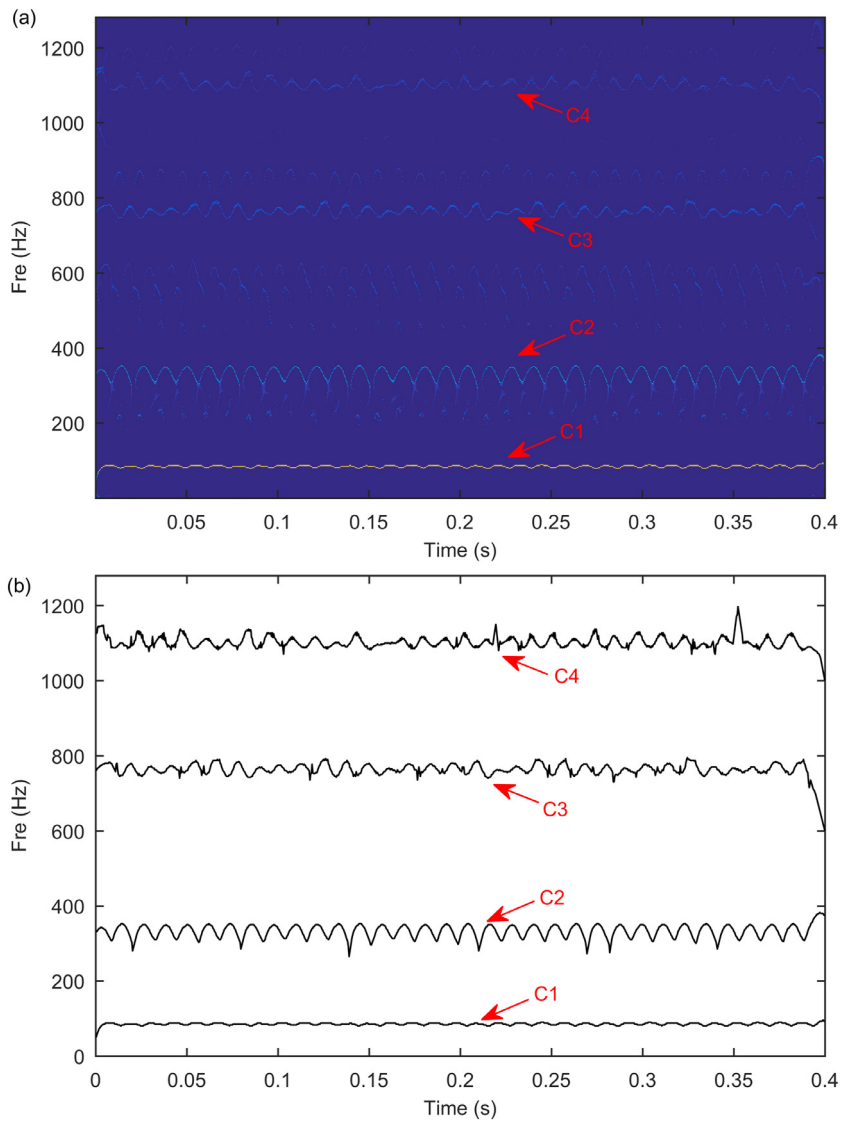


Fig. 22. (a) IMSST result and (b) the detected IF trajectories.

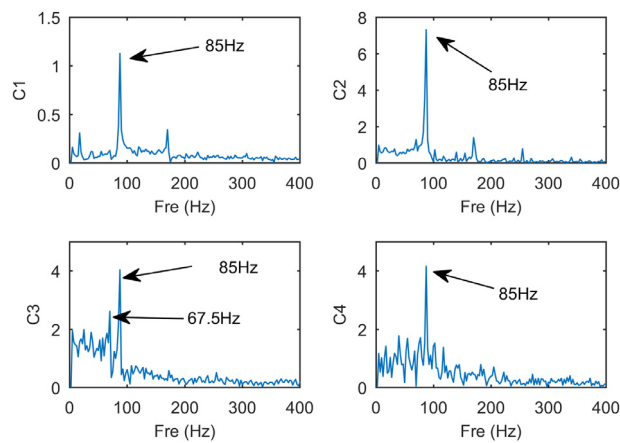


Fig. 23. The spectrum of four detected IFs.

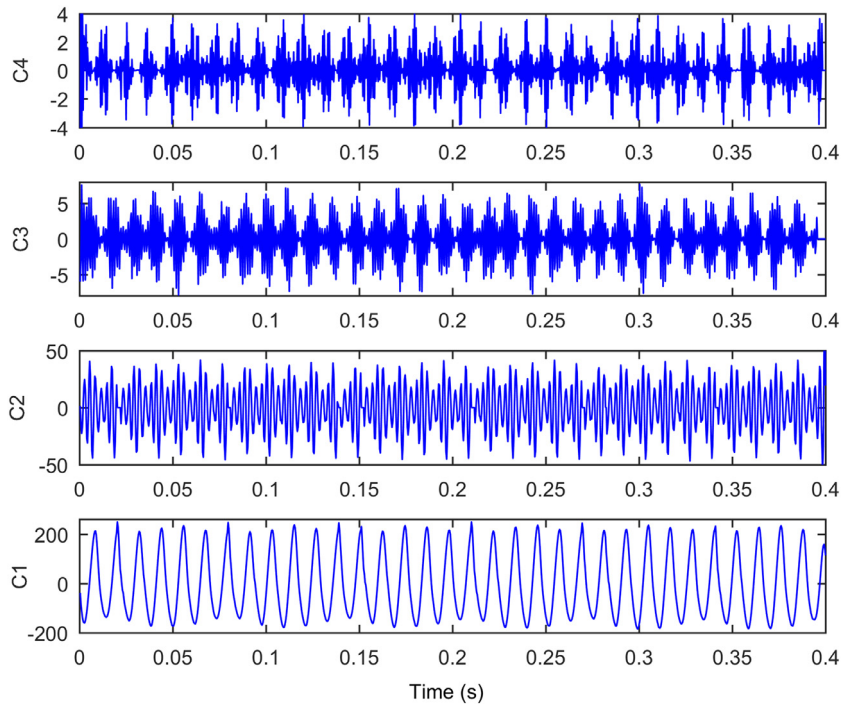


Fig. 24. Waveform of the four reconstructed components.

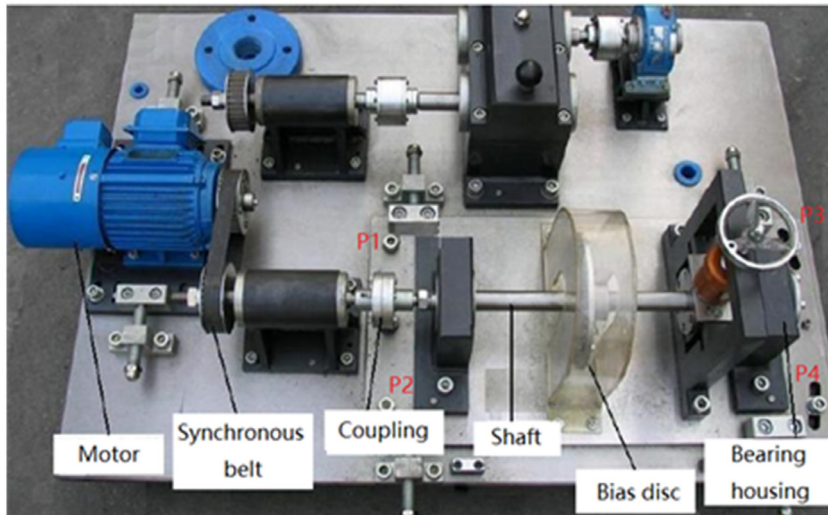
eventually leads to the appearance of periodic transient features. A total of 34 transients appear in the waveforms of C3 and C4, which is consistent with the rotation number of the rotor within 0.4 s.

From the above analysis, it is known that the vibration signal of the rotor system with a rub impact fault consists of multiple components closely related to the rotating frequency. The low frequency components, e.g., C1 and C2, often have large amplitudes and relatively harmonic waveforms. In each rotation, when the rotor passes through the fault position, local deceleration and acceleration effects are introduced to the speed of the shaft. Thus, the IF trajectories of all components exhibit periodically oscillating characteristics. Additionally, the rub impact fault has an AM effect on the rotor, which eventually leads to the obvious transient features of the high frequency components, e.g., C3 and C4. The transient features in the vibration signal recorded from a rotating machine usually indicate the appearance of an early fault [34]. Therefore, we should not only analyze the components with large amplitudes, but also pay more attention to the weak components in the high frequency band. The weak components are often more closely related to the early faults of a rotating machine.

4.3. Two vibration signals of a rotating machine with an outer race fault and inner race fault under variable speed conditions

In practical engineering, the vibration signal recorded from rotating machinery under variable speed conditions usually tends to have high FM and AM trends [37–39]. The conventional methods usually cannot work well in such situations. To illustrate the effectiveness of the IMSST method for bearing fault diagnosis under variable speed conditions, two experiments are carried out with a machinery fault simulator (see Fig. 25). Two faults are introduced to the bearing outer race and inner race via wire cutting, which is shown in Fig. 25(b–c). The type of the test bearing is SKF 6205. An accelerometer and an inductive sensor are used to record the vibration signals and the rotating frequency (RF). For a bearing fault vibration signal, because the moving part of the bearing repeatedly passes through the fault location, a series of impulsive components appear at a certain frequency called the fault characteristic frequency (FCF) [40–42]. The interval between two successive impulsive components is determined by the RF and the fault type. According to the parameters of the bearing SKF 6205, the ratio of the FCFs of the outer race fault and the inner race fault with respect to the RF should be 3.584 and 5.416, respectively.

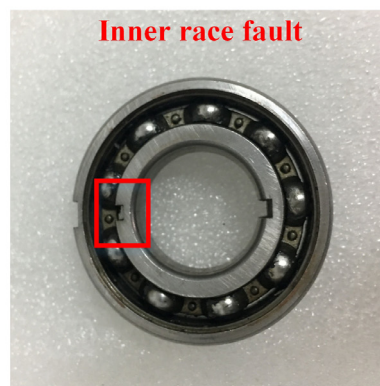
The vibration signal of the rotating machinery with the bearing outer race fault is first analyzed. Fig. 26 shows the vibration signal and the RF, where the sampling frequency and sampling time are 20 kHz and 5 s, respectively. It is shown that the RF increases from 27.5 Hz to 40 Hz, then decreases to 32 Hz. The signal amplitude has a trend similar to that of the RF. It is known that the FCF is often calculated from the envelope of the vibration signal. The envelope signal is shown in Fig. 27(a). The IMSST results for the envelope signal during 0.5 s – 1 s and 3 s – 3.5 s are respectively provided in Fig. 27(b) and (c). It is obvious that the time-varying outer fault FCF (denoted as F_o) and its high-order components ($2F_o$, $3F_o$ and $4F_o$) are clearly characterized by the concentrated TFR.



(a)



(b)



(c)

Fig. 25. (a) Structural sketch of the machine set, (b) outer race fault and (c) inner race fault.

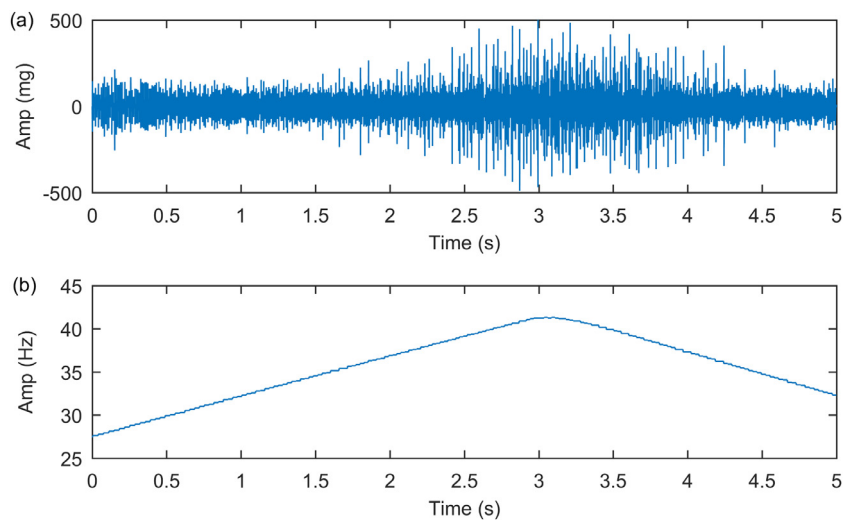


Fig. 26. (a) Vibration signal and (b) rotating frequency.

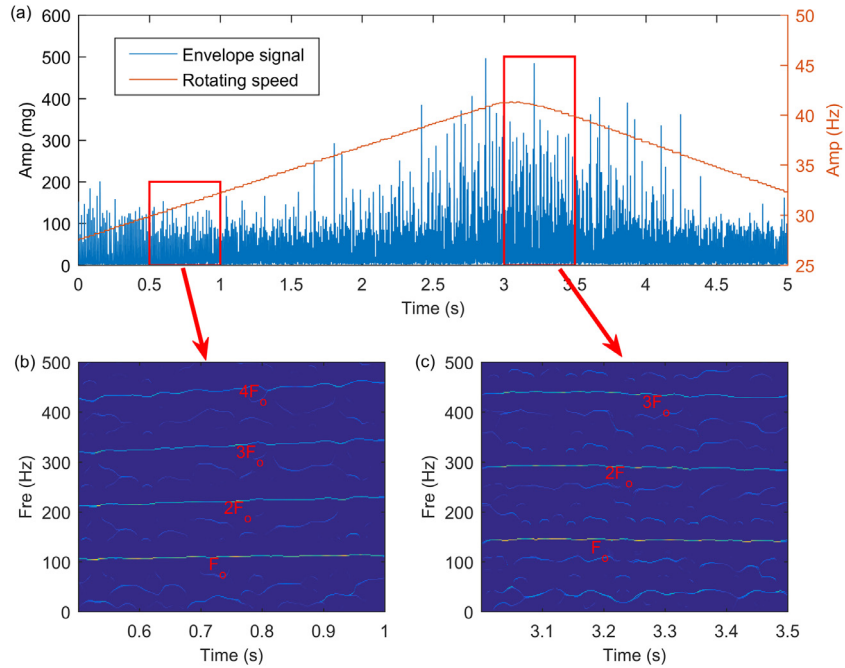


Fig. 27. (a) Envelope of the vibration signal, (b) the IMSST result for 0.5 s - 1 s and (c) the IMSST result for 3 s - 3.5 s.

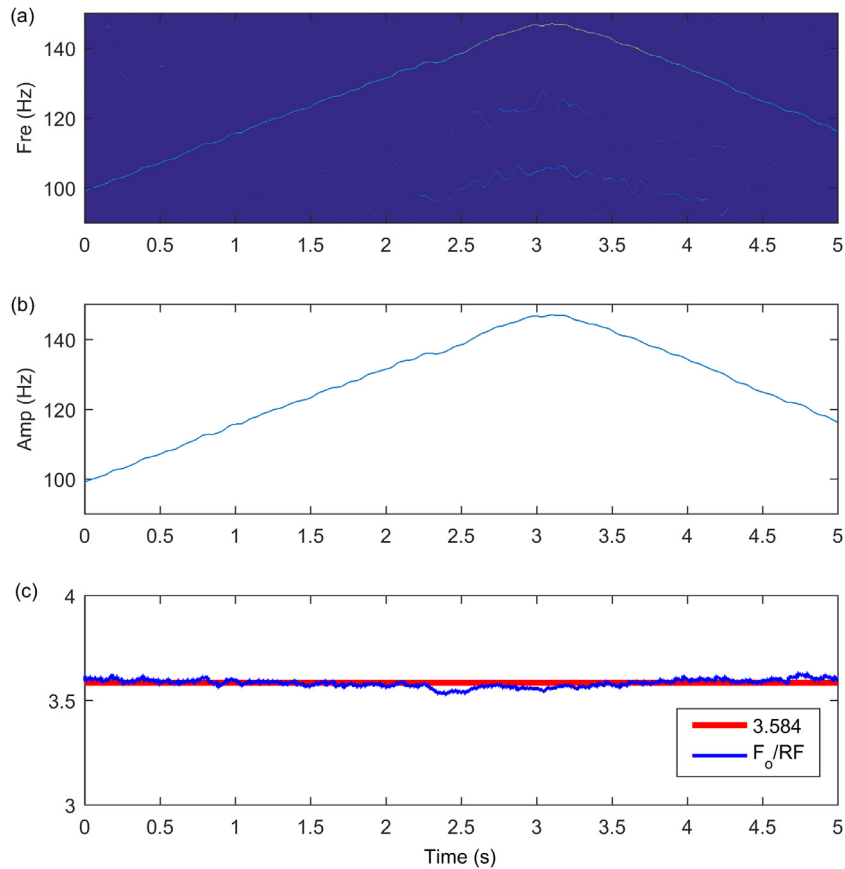


Fig. 28. (a) IMSST result within the frequency band 90 Hz - 150 Hz, (b) the estimated trajectory and (c) F_0/RF .

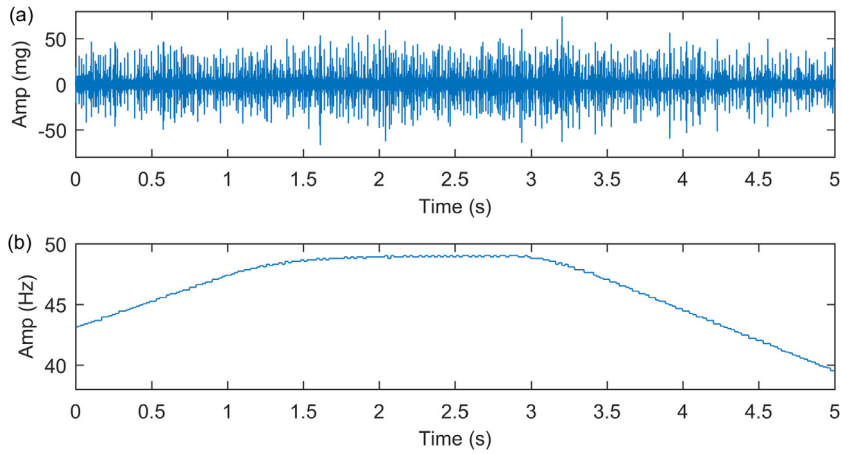


Fig. 29. (a) Vibration signal and (b) rotating frequency.

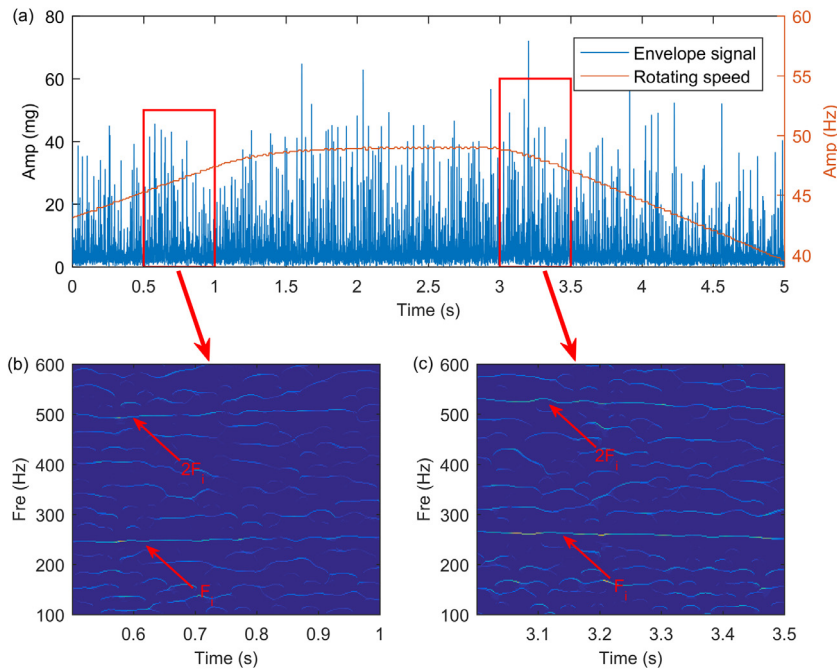


Fig. 30. (a) Envelope of the vibration signal, (b) the IMSST result for 0.5 s - 1 s and (c) the IMSST result for 3 s - 3.5 s.

In theory, the ratio of the first-order outer fault FCF with respect to the RF is 3.584. We mainly focus on the TFR within the frequency band of 90 Hz - 150 Hz (see Fig. 28(a)). The IMSST clearly characterizes the time-varying features of the first-order outer fault FCF. The related trajectory estimated by the ridge detection algorithm is also plotted in Fig. 28(b). The ratio of the time-varying FCF to RF (i.e., F_0/RF) is plotted in Fig. 28(c). It can be seen that the trajectory of the F_0/RF is highly accordant with the theoretical value.

The second experiment of the bearing inner race fault is carried out, which is plotted in Fig. 29. The RF first increases from 43 Hz to 49 Hz, and then decreases to 39 Hz. The envelope of the vibration signal and the TFRs are shown in Fig. 30. Compared with the outer race fault signal, although the inner race fault signal contains more unexpected noise, the time-varying FCF and its high-order components are clearly characterized. The TFR of the first-order FCF and its trajectory are displayed in Fig. 31(a) and (b). Fig. 31(c) shows that the ratio of the inner fault FCF to RF (i.e., F_1/RF) is also highly accordant with the theoretical value. Both two experiments illustrate the effectiveness of the IMSST method in dealing with vibration signals under variable speed. With the aid of the concentrated TFA technique, it is possible to obtain more precise information for bearing fault diagnosis.

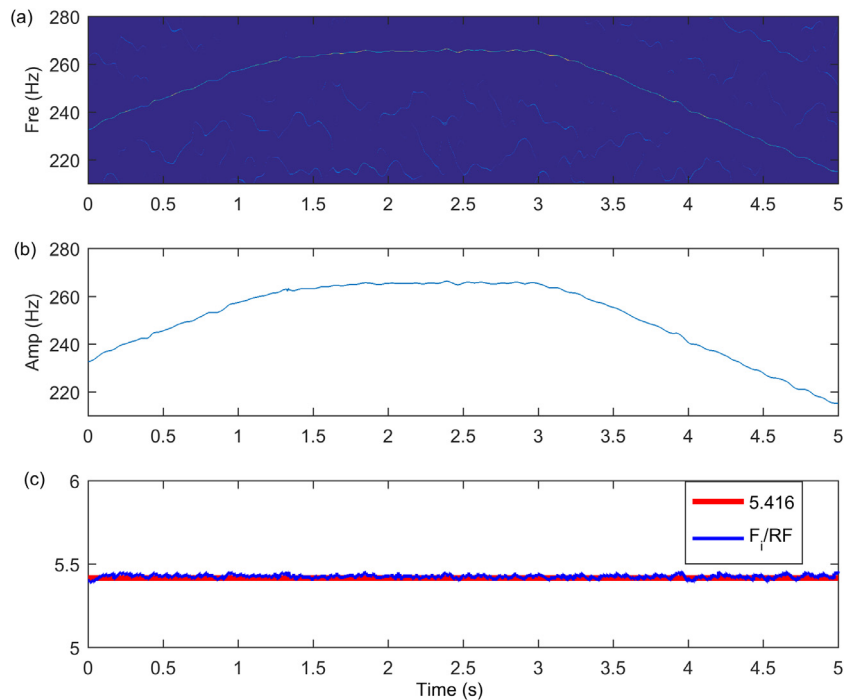


Fig. 31. (a) IMSST result within the frequency band 210 Hz – 280 Hz, (b) the estimated trajectory and (c) F_i/RF .

5. Conclusion

In this paper, the occurrence of the non-reassigned point problem of the MSST method is first explored, and then an effective method is proposed for resolving this problem. Finally, a highly concentrated TFA method is established, which is termed the IMSST. The proposed method has better capacity to address a wide variety of time-varying signals even containing strong noise. Numerical and experimental signals are employed to illustrate the advantage of the proposed method through comparison with other techniques. The validations demonstrate that, with the benefit of the concentrated TF features, it is possible to recognize the complex time-varying signals and the underlying physical phenomenon. A MATLAB implementation of the proposed algorithm is available at <https://www.mathworks.com/matlabcentral/fileexchange/81763>.

Declaration Of Competing Interest

I would like to declare that the work described was original research that has not been published previously, and not under consideration for publication elsewhere, in whole or in part.

CRedit authorship contribution statement

Gang Yu: Conceptualization, Methodology, Validation, Writing - original draft, Writing - review & editing.

Acknowledgments

This work was supported by National Natural Science Foundation of China under Grant 61901190. The author is grateful to Pro. Guo Chen from Nanjing University of Aeronautics and Astronautics, Dr. Kun Yu and Pro. Hui Ma from Northeastern University for sharing their experimental data.

References

- [1] J. Wang, Q. He, F. Kong, An improved multiscale noise tuning of stochastic resonance for identifying multiple transient faults in rolling element bearings, *J. Sound Vib* 333 (2014) 7401–7421.
- [2] J. Wang, Q. He, F. Kong, An improved multiscale noise tuning of stochastic resonance for identifying multiple transient faults in rolling element bearings, *J. Sound Vib* 333 (2014) 7401–7421.
- [3] F. Chu, W. Lu, Experimental observation of nonlinear vibrations in a rub-impact rotor system, *J. Sound Vib* 283 (2005) 621–643.
- [4] Z. Peng, F. Chu, Application of the wavelet transform in machine condition monitoring and fault diagnostics: a review with bibliography, *Mech. Syst. Signal Process.* 18 (2004) 199–221.
- [5] F.F. Ehrich, High order subharmonic response of high speed rotors in bearing clearance, *ASME J. Vibr. Acoust. Stress Reliab. Des* 110 (1) (1988) 9–16.

- [6] P. Pennacchi, N. Bachschmid, E. Tanzi, Light and short arc rubs in rotating machines: experimental tests and modelling, *Mech. Syst. Signal Process.* 23 (2009) 2205–2227.
- [7] H. Ma, C. Shi, Q. Han, B. Wen, Fixed-point rubbing fault characteristic analysis of a rotor system based on contact theory, *Mech. Syst. Signal Process.* 38 (2013) 137–153.
- [8] Z. Feng, M. Liang, F. Chu, Recent advances in time–frequency analysis methods for machinery fault diagnosis: A review with application examples, *Mech. Syst. Signal Process.* 38 (2013) 165–205.
- [9] J. Chen, Z. Li, J. Pan, et al., Wavelet transform based on inner product in fault diagnosis of rotating machinery: A review, *Mech. Syst. Signal Process.* 70 (2016) 1–35.
- [10] Y. Yang, Z. Peng, W. Zhang, et al., Parameterised time-frequency analysis methods and their engineering applications: A review of recent advances, *Mech. Syst. Signal Process.* 119 (2019) 182–221.
- [11] F. Auger, P. Flandrin, Y.T. Lin, et al., Time-frequency reassignment and synchrosqueezing: An overview, *IEEE Signal Process. Mag.* 30 (2013) 32–41.
- [12] F. Auger, P. Flandrin, Improving the readability of time–frequency and time–scale representations by the reassignment method, *IEEE Trans. signal process.* 43 (1995) 1068–1089.
- [13] I. Daubechies, J. Lu, H.T. Wu, Synchrosqueezed wavelet transforms: an empirical mode decomposition-like tool, *Appl. Comput. Harmon. Anal.* 30 (2011) 243–261.
- [14] G. Thakur, E. Brevdo, N.S. Fućkar, et al., The synchrosqueezing algorithm for time-varying spectral analysis: Robustness properties and new paleoclimate applications, *Signal process* 93 (2013) 1079–1094.
- [15] Y. Yang, W. Zhang, Z. Peng, et al., Multicomponent signal analysis based on polynomial chirplet transform, *IEEE Trans. Ind. Electron.* 60 (2013) 3948–3956.
- [16] S. Wang, X. Chen, G. Cai, et al., Matching demodulation transform and synchrosqueezing in time-frequency analysis, *IEEE Trans. Signal Process.* 62 (2014) 69–84.
- [17] X. Tu, Y. Hu, F. Li, et al., Demodulated High-Order Synchrosqueezing Transform With Application to Machine Fault Diagnosis., *IEEE Trans. Ind. Electron.* 66 (2019) 3071–3081.
- [18] T. Oberlin, S. Meignen, V. Perrier, Second-order synchrosqueezing transform or invertible reassignment? Towards ideal time-frequency representations, *IEEE Trans. Signal Process* 63 (2015) 1335–1344.
- [19] D.H. Pham, S. Meignen, High-order synchrosqueezing transform for multicomponent signals analysis—With an application to gravitational-wave signal, *IEEE Trans. Signal Process.* 65 (2017) 3168–3178.
- [20] G. Yu, M. Yu, C. Xu, Synchroextracting transform, *IEEE Trans. Ind. Electron.* 64 (2017) 8042–8054.
- [21] G. Yu, Z. Wang, P. Zhao, et al., Local maximum synchrosqueezing transform: An energy-concentrated time-frequency analysis tool, *Mech. Syst. Signal Process* 117 (2019) 537–552.
- [22] G. Yu, Z. Wang, P. Zhao, Multisynchrosqueezing Transform, *Trans. Ind. Electron.* 66 (2019) 5441–5455.
- [23] C. Li, M. Liang, Time–frequency signal analysis for gearbox fault diagnosis using a generalized synchrosqueezing transform, *Mech. Syst. Signal Process.* 26 (2012) 205–217.
- [24] Z. Feng, X. Chen, M. Liang, Iterative generalized synchrosqueezing transform for fault diagnosis of wind turbine planetary gearbox under nonstationary conditions, *Mech. Syst. Signal Process.* 52 (2015) 360–375.
- [25] R.H. Herrera, J. Han, M. van der Baan, Applications of the synchrosqueezing transform in seismic time-frequency analysis, *Geophysics* 79 (2014) V55–V64.
- [26] Z. Huang, J. Zhang, T. Zhao, et al., Synchrosqueezing S-transform and its application in seismic spectral decomposition, *IEEE Trans. Geosci. Remote Sens.* 54 (2015) 817–825.
- [27] H.T. Wu, Y.H. Chan, Y.T. Lin, et al., Using synchrosqueezing transform to discover breathing dynamics from ECG signals, *Appl. Comput. Harmon. Anal.* 36 (2014) 354–359.
- [28] L. Stanković, I. Djurović, S. Stanković, et al., Instantaneous frequency in time–frequency analysis: Enhanced concepts and performance of estimation algorithms, *Digital Signal Process* 35 (2014) 1–13.
- [29] G. Chen, J. Chen, G. Dong, et al., An adaptive non-parametric short-time Fourier transform: application to echolocation, *Applied Acoustics* 87 (2015) 131–141.
- [30] V. Susic, N. Saulig, B. Boashash, Estimating the number of components of a multicomponent nonstationary signal using the short-term time-frequency Rényi entropy, *EURASIP Journal on Advances in Signal Processing* 2011 (2011) 125.
- [31] S. Meignen, T. Oberlin, S. McLaughlin, A new algorithm for multicomponent signals analysis based on synchrosqueezing: With an application to signal sampling and denoising, *IEEE trans. Signal Process.* 60 (2012) 5787–5798.
- [32] S. Chen, M. Du, Z. Peng, et al., High-accuracy fault feature extraction for rolling bearings under time-varying speed conditions using an iterative envelope-tracking filter, *J. Sound Vib.* 448 (2019) 211–229.
- [33] S. Chen, Y. Yang, Z. Peng, et al., Detection of rub-impact fault for rotor-stator systems: A novel method based on adaptive chirp mode decomposition, *J. Sound Vib.* 440 (2019) 83–99.
- [34] H. Ma, T. Yu, Q. Han, et al., Time–frequency features of two types of coupled rub-impact faults in rotor systems, *J. Sound Vib.* 321 (2009) 1109–1128.
- [35] H. Ma, C. Shi, Q. Han, et al., Fixed-point rubbing fault characteristic analysis of a rotor system based on contact theory, *Mech. Syst. Signal Process.* 38 (2013) 137–153.
- [36] G. Chen, Study on nonlinear dynamic response of an unbalanced rotor supported on ball bearing, *J. Vib. Acoust.* 131 (2009) 061001.
- [37] W. Huang, G. Gao, N. Li, et al., Time-Frequency Squeezing and Generalized Demodulation Combined for Variable Speed Bearing Fault Diagnosis, *IEEE Trans. Instrum. Meas.* 68 (2018) 2819–2829.
- [38] J. Shi, M. Liang, D.S. Neculescu, et al., Generalized stepwise demodulation transform and synchrosqueezing for time–frequency analysis and bearing fault diagnosis, *J. Sound Vib.* 368 (2016) 202–222.
- [39] Y. Guan, M. Liang, D.S. Neculescu, Velocity synchronous bilinear distribution for planetary gearbox fault diagnosis under non-stationary conditions, *J. Sound Vib.* 443 (2019) 212–229.
- [40] H. Huang, N. Baddour, M. Liang, Bearing fault diagnosis under unknown time-varying rotational speed conditions via multiple time-frequency curve extraction, *J. Sound Vib.* 414 (2018) 43–60.
- [41] H. Huang, N. Baddour, M. Liang, A method for tachometer-free and resampling-free bearing fault diagnostics under time-varying speed conditions, *Meas.* 134 (2019) 101–117.
- [42] J. Zheng, H. Pan, T. Liu, et al., Extreme-point weighted mode decomposition, *Signal Process.* 142 (2018) 366–374.